IEEE Access
Multidisciplinary | Rapid Review | Open Access Journal

Date of publication xxxx 00, 0000, date of current version xxxx 00, 0000.

Digital Object Identifier 10.1109/ACCESS.2024.Doi Number

Multi-band Torsional Vibration Amplitude Demodulation for Planetary Gearbox Fault Diagnosis under Time–varying Speed Conditions

Xiaowang Chen, Yubo Sun, Ying Zhang, Member, IEEE, and Zhipeng Feng, Member, IEEE
School of Mechanical Engineering, University of Science and Technology Beijing, Beijing 100083, China

Corresponding author: Zhipeng Feng (e-mail: fengzp@ustb.edu.cn).

ABSTRACT Torsional vibration signal analysis is promising for diagnosing gear faults in planetary gearboxes. However, early-stage fault signatures are relatively-weak and may be ignored or wrongly identified in conventional demodulation analysis, especially under time-varying speed conditions. Two main contributions are made in this paper. Firstly, an analytical model of planetary gearbox torsional vibration signal is established, by jointly considering the gear mesh vibration, torsional resonance, and other time-invariant components. The gear fault characteristics under time-varying speeds are accordingly revealed explicitly. Furthermore, inspired by the unique time-frequency structure of the torsional vibration signal, the multi-band torsional vibration amplitude demodulation method is proposed for gear fault feature extraction. The proposed method combines the gear fault features in multiple characteristic frequency bands in torsional vibration signal, so that the influences from adjacent carrier frequencies, independent frequency harmonics and random noises can be eliminated in amplitude demodulation. As a result, the obtained amplitude demodulated order spectrum outperforms conventional envelope order spectrum and narrow-band amplitude demodulated order spectrum in revealing relatively weak gear fault features. Both numerical simulation and laboratory experiments are conducted, to demonstrate the correctness of the established analytical model and the advantages of the proposed multi-band torsional vibration amplitude demodulation method. Localized fault on the sun, planet and ring gears are successfully diagnosed.

INDEX TERMS Analytical model, fault diagnosis, planetary gearbox, resonance demodulation, torsional vibration.

I. INTRODUCTION

Planetary gearboxes are extensively applied in various equipment in aerospace, mining, energy, and many other fields. Due to heavy load and volatile operating conditions, the gear teeth transmit large alternating torque and are prone to fault. The undetected planetary gearbox fault results in reduced efficiency, harsh noises, and even unscheduled shutdown of the whole equipment. Therefore, effective diagnosis of planetary gearbox fault is of significance for ensuring safe and smooth industrial activities [1]-[3]. Comparing with traditional fixed-shaft gearbox, planetary gearboxes have much more complex vibration response due to multiple gear pairs meshing under different phase angles and time-varying vibration transmission paths. The resulting joint amplitude modulation and frequency modulation structure leaves the fault feature extraction challenging.

Torsional vibration analysis is promising for diagnosing planetary gearbox fault [4]-[6]. Since the damaged gear tooth leads to abnormality of the mesh stiffness, the magnitude of torsional vibration response changes when the damaged gear tooth meshes with the mating gear. Therefore, the amplitude envelope and instantaneous frequency of the torsional vibration signal periodically changes at the gear fault frequency. By detecting the fault-related frequency components in the measured torsional vibration signal, different gear faults can be recognized and located.

Furthermore, torsional vibration analysis has appealing merits over the commonly used transverse vibration analysis for planetary gearbox fault feature extraction.

Owing to the unique measuring method, torsional vibration signals are free from the modulation effects by time-varying vibration transmission paths in transverse direction. When gear fault occurs on the sun gear or planet gear, the gear fault meshing locations revolves around the geometric center of the sun gear. Such unique gear motion leads to periodically changing vibration transmission paths between the gear fault meshing location and the fixed accelerometer on gearbox casing. As a result, the measured transverse vibration signal is additionally amplitude modulated by the revolving frequency [8]. On the contrary, the radial distance between the gear fault meshing location and the torque transducer connected to the rotating shaft remains unchanged. The revolving fault meshing locations therefore does not cause extra amplitude modulation on the measured torsional vibration signal, and the relatively simpler signal modulation structure facilitates the planetary gearbox fault feature extraction.

However, inadequate attention has so far been paid on the research of torsional vibration-based planetary gearbox fault diagnosis. Available references mostly focus on discovering the fault characteristics in transverse vibration signals. Feng and Zuo [8] exploited the signal analytical modeling strategy to reveal the distribution of fault-induced frequency sidebands in transverse vibration signal. Lei et al. [9] analyzed the influence of unequally spaced planet gears on the planetary gearbox transverse vibration signals and found that additional frequency components may occur and further complicate the frequency structure. He et al. [10] interpreted the planetary gearbox transverse vibration signals with mathematical model, by studying the time-varying transmission paths and meshing force direction. Nevertheless, the gear fault characteristics in measured transverse vibration signals may not be adaptable to the measured torsional vibration signals, because the vibration responses and vibration transmission paths in transverse or torsional direction are different.

Besides, thorough understanding of torsional vibration characteristics in various frequency regions and under nonstationary operational conditions is still missing. Published works of torsional vibration-based planetary gearbox fault diagnosis mostly focus on fault characteristics in gear meshing frequency band under steady speed conditions. Feng and Zuo [11] extended the transverse vibration signal model of planetary gearbox to torsional direction, and analytically derived the fault modulation frequency features distributed around the gear meshing frequency. Xue and Howard [5] calculated the planetary gearbox mesh stiffness using the finite element method, and further integrated it with lumped parameter model to numerically simulated the torsional vibration response under fixed operating speed. These works provide valuable guidance for torsional vibration-based planetary gearbox fault diagnosis, yet only the time-invariant frequency characteristics in gear meshing frequency regions are discussed. The characteristic frequency sidebands around the torsional resonance frequencies also contain meaningful gear fault features [12], and proper utilization of fault characteristics in different frequency regions may improve the accuracy of planetary gearbox fault feature extraction. A more general mathematically interpretation of the measured planetary gearbox torsional vibration signal still deserves further research.

Effective fault feature extraction from the measured torsional vibration signal is another essential topic for planetary gearbox fault diagnosis. The envelope spectrum analysis is one of the most widely used method for gear fault detection, since it is capable of directly revealing the amplitude modulation frequency components in relatively low frequency band [13-14]. Narrow-band amplitude demodulation analysis resembles envelope spectrum analysis, but it theoretically focuses on only one carrier frequency region [15-16], and other frequency features are filtered out beforehand for avoiding unwanted interferences. Xue and Howard [5] tried different demodulation frequency bands and found that the amplitude modulation features around the 4th gear meshing frequency harmonic are most sensitive to the analyzed gear faults. Wang [17] removed the gear meshing frequency harmonics and analyzed the residual resonance demodulation features for detecting gear teeth crack. Chen et al. [12] focused on the relatively high torsional resonance frequency band and identified the time-varying fault frequency sidebands.

However, neither envelope spectrum analysis nor narrow-band amplitude demodulation analysis makes full utilization of the fault characteristics distributed in different frequency regions. Envelope spectrum analysis theoretically only fits for revealing amplitude modulation features of mono-component signals, and its performance deteriorates as the frequency structure of the analyzed signal becomes complex. For planetary gearbox torsional vibration signals, the fault modulation frequency components distribute around the gear meshing frequency harmonics, the torsional resonance frequency components, and probably other characteristic frequency components caused by the measurement devices. The differences between carrier frequencies or independent rotating frequency orders therefore may be misjudged as modulation frequencies. Besides, the narrow-band demodulation analysis essentially omits the existing fault features in the unselected frequency bands, and the universal criterion for selecting the optimal demodulation frequency band is still unavailable [16], especially under time-varying speed conditions.

In summary, ambiguous fault feature distribution and inadequate utilization of the modulation details hinder the torsional-vibration-based planetary gearbox fault diagnosis under time-varying speed conditions. In this work, two main contributions are made to address the abovementioned issues. Firstly, the analytical model of

planetary gearbox torsional vibration signal under local gear fault condition is established. The scope of the proposed signal analytical model covers torsional vibration features in various frequency regions under time-varying speed conditions. The fault-modulated gear mesh vibration features, fault-modulated torsional resonance features, and other characteristic frequency components caused by the measurement devices are jointly considered and analytically derived to provide complete understanding of the torsional vibration characteristics. Secondly, the multi-band torsional vibration amplitude demodulation method is proposed for gear fault extraction. Its novelty lies in joint utilization of fault features in different torsional vibration frequency regions and meanwhile suppress the random interferences. Comparing with the conventional envelope spectrum and narrow-band amplitude demodulation analysis, the proposed method enables clearer fault feature revelation for more accurate fault diagnosis.

The remainder of this manuscript is structured as follows. In Section 2, the analytical model of the torsional vibration signal measured from a single-stage planetary gearbox is established. Based on the analytical interpretation of torsional vibration characteristics in different frequency regions, the multi-band torsional vibration amplitude demodulation method is proposed in Section 3. Numerical simulation analysis and laboratory experimental signal analysis are respectively conducted in Section 4 and 5, to validate the correctness of the established signal analytical model, and to demonstrate the merits of the proposed method. Conclusions are finally drawn in Section 6.

II. Analytical Modelling of Torsional Vibration Signal

In this section, the measured torsional vibration signal of a single-stage planetary gearbox is elaborated and analytically modeled. The ring gear of the planetary gearbox is set fixed, and the sun gear is used as the input. Without loss of generality, the operating speed is time-varying.

A. Fault-modulated torsional gear mesh vibration

The time-varying gear mesh stiffness of the sun-planet and planet-ring gear meshing pairs cause torsional vibration at gear meshing frequency $f_{\mathrm{m}}(t)$. It can be calculated by

$$f_{\mathrm{m}}(t) = f_{\mathrm{c}}^{(\mathrm{r})}(t)\,Z_{\mathrm{r}} = [\,f_{\mathrm{s}}^{(\mathrm{r})}(t) - f_{\mathrm{c}}^{(\mathrm{r})}(t)]\,Z_{\mathrm{s}}\,, \tag{1}$$

where Z_{r} and Z_{s} respectively indicates the number of teeth of the ring gear and the sun gear, $f_{\mathrm{s}}^{(\mathrm{r})}(t)$ and $f_{\mathrm{c}}^{(\mathrm{r})}(t)$ are the rotating frequencies of the sun gear and the planet carrier. The rotating frequency of planet gear (with number of teeth Z_{p}) is denoted by $f_{\mathrm{p}}^{(\mathrm{r})}(t)$ in the following.

When localized gear fault occurs, the gear mesh stiffness changes once the faulty gear tooth meshes with its mating gear. The amplitude envelope of the generated torsional gear mesh vibration signal therefore periodically changes at the gear fault frequency. Besides, the instantaneous frequency of the torsional gear mesh vibration signal changes when abnormity occurs, and the gear mesh frequency reappears when the faulty gear tooth is no longer in mesh. Therefore, the torsional gear mesh vibration is jointly amplitude modulated (AM) and frequency modulated (FM) by the gear fault frequency. For simplicity, the sun gear fault frequency $f_{\mathrm{s}}(t)$, planet gear fault frequency $f_{\mathrm{p}}(t)$, and ring gear fault frequency $f_{\mathrm{c}}(t)$ are uniformly written as gear fault frequency $f_{\mathrm{g}}(t)$. Calculations of different gear fault frequencies can be found in [4]. Considering the harmonics of gear mesh frequency at order k=1, 2, 3⋯, the fault-modulated torsional gear mesh vibration signal $S_{\mathrm{m}}(t)$ can be cast as

$$S_{\mathrm{m}}(t) = \sum_{k=1}^{\infty} c_{\mathrm{m}k}(t)\,a_{\mathrm{m}k}(t)\cos[2\pi\textstyle\int k f_{\mathrm{m}}(t)\mathrm{d}t + b_{\mathrm{m}k}(t) + \psi_{\mathrm{m}k}]\,, \tag{2}$$

where $c_{\mathrm{m}k}(t)$ indicates the time-varying amplitude response, and $a_{\mathrm{m}k}(t)$, $b_{\mathrm{m}k}(t)$ respectively stands for the amplitude and frequency modulation term, expanded as

$$a_{\mathrm{m}k}(t) = 1 + \sum_{n=0}^{\infty} A_{\mathrm{mg}kn}(t)\cos[2\pi\textstyle\int n f_{\mathrm{g}}(t)\mathrm{d}t + \varphi_{\mathrm{mg}kn}]\,, \tag{3}$$

$$b_{\mathrm{m}k}(t) = \sum_{l=0}^{\infty} B_{\mathrm{mg}kl}(t)\cos[2\pi\textstyle\int l f_{\mathrm{g}}(t)\mathrm{d}t + \gamma_{\mathrm{mg}kl}]\,. \tag{4}$$

The modulation coefficients $A_{\mathrm{mg}kn}(t)$ and $B_{\mathrm{mg}kl}(t)$ are determined by the gearbox dynamics and fault severity, and vary at different fault frequency harmonics at order n or l. $\psi_{\mathrm{m}k}$, $\varphi_{\mathrm{mg}kn}$ and $\gamma_{\mathrm{mg}kl}$ are the corresponding initial phases.

According to the identity of Bessel functions [18]

$$\exp[\,jz\sin(\theta)] = \sum_{q=-\infty}^{\infty} J_q(z)\exp(jq\theta)\,, \tag{5}$$

the torsional gear mesh vibration can be rewritten as

$$S_{\mathrm{m}}(t) = \sum_{k=1}^{\infty} c_{\mathrm{m}k}(t)\,a_{\mathrm{m}k}(t) \sum_{q=-\infty}^{\infty}\sum_{l=0}^{\infty}\Big\{J_q[B_{\mathrm{mg}kl}(t)] \cos\Big\{2\pi\textstyle\int[k f_{\mathrm{m}}(t) + q l f_{\mathrm{g}}(t)]\mathrm{d}t + \psi_{\mathrm{m}k} + q\gamma_{\mathrm{mg}kl}\Big\}\Big\}\,, \tag{6}$$

and its frequency compositions include a summation of time-varying frequency components located at gear mesh frequency harmonics $kf_{\mathrm{m}}(t)$, as well as their upper and lower frequency sidebands with interval of gear fault frequency $f_{\mathrm{g}}(t)$, as $|kf_{\mathrm{m}}(t)\pm hf_{\mathrm{g}}(t)|$ (h=0, 1, 2⋯). The amplitude $AP_{\mathrm{mg}kh}(t)$ of fault frequency component $|kf_{\mathrm{m}}(t)\pm hf_{\mathrm{g}}(t)|$ can be estimated by

$$AP_{\mathrm{mg}kh}(t) = c_{\mathrm{m}k}(t)\Big\{\frac{1}{2}A_{\mathrm{mg}kh}(t) + J_1[B_{\mathrm{mg}kh}(t)] + J_h[B_{\mathrm{mg}k1}(t)] + \frac{z}{2}A_{\mathrm{mg}kh_1}(t)J_{h_3}[B_{\mathrm{mg}kh_2}(t)]\Big\}\,, \tag{7}$$

where z denotes the number of integer arrays (h_1, h_2, h_3) which fulfills $h_2h_3\pm h_1=h$. It is worth noticing that the Bessel functions in (7) often have small value, so the amplitude of fault

frequency sideband depend much on the amplitude $c_{mk}(t)$ and amplitude modulation coefficient $A_{mgkn}(t)$.

To avoid the identification of complex modulation sidebands, amplitude demodulation is often conducted to directly extract and analyze the time-frequency characteristics of the amplitude modulation term $a_{mk}(t)$. According to (3), the time-varying gear fault frequency and its harmonics are expected in the amplitude envelope signal of the torsional gear mesh vibration.

B. Fault-induced torsional resonance vibration

The planetary gearbox torsional resonance characteristics have seldom been elaborated in available publications, especially when the rotating speed is time-varying. When local gear fault such as gear tooth crack exist, short-duration impact will occur once the faulty gear tooth gets into mesh. The impact excites structural resonance vibration in torsional direction, and convolutes the transfer function (i.e., the frequency response function). For a single faulty gear tooth mesh, the generated torsional resonance vibration signal $S_r(t)$ can be modeled as [17]

$$S_r(t) = c_r(t)\cos[2\pi f_r t + \psi_r], \tag{8}$$

where f_r denotes the torsional resonance frequency, and ψ_r is the initial phase. $c_r(t)$ stands for the amplitude envelope of the resonant vibration, and is decided by the impulse response of the system. Since the dynamic characteristics of the planetary gearbox system is often complex and unknown, the fast-decaying characteristics of the amplitude envelope under damped condition is modeled as $c_r(t)=c_r\exp\{-2\pi\beta f_n t\}$, where $f_n^2= f_r^2/(1-\beta^2)$, and β denotes the damping ratio.

Under time-varying rotating speed conditions, the fault impacts are generated repeatedly at the gear fault frequency $f_g(t)$. Equation (8) is then rewritten as

$$S_r(t) = \sum_{i=1}^{\infty} c_r(t-t_i)\cos[2\pi f_r(t-t_i)+\psi_{ri}], \tag{9}$$

where i denotes the index of fault impacts. As a result, the torsional resonance vibration theoretically covers the full-spectrum-band, but have amplified energy in the vicinity of the resonance frequency [19-20]. To directly reveal the fault signatures, the amplitude demodulation analysis is performed to focus on the characteristics of the amplitude envelope. According to (9), the time-varying gear fault frequency and its harmonics can be revealed in the amplitude envelope signal of the torsional resonance vibration.

C. Other components in the measured signal

In real-world measurements, electric signal components resulted from the measurement devices may exist in the measured torsional vibration signal. For example, if an active rotary torque transducer is used to measure the torque signal from a rotating shaft, the alternating voltage source added on the rotary transformer results in extra frequency components in the measured signal. Besides, the electric signal components from the power grid or inverter, as well as the related modulation sidebands, may also occur in the measured signal if the device is not properly grounded. The oscillating frequencies of these components are decided by their sources, and do not change under time-varying speed conditions. On the other hand, their amplitudes are affected by the structural behavior, and further be modulated by the fault-induced dynamic change [10]. Analyses of these fault characteristics also help diagnose the planetary gearbox fault.

These carrier frequencies are denoted as f_{de} (e =1, 2, 3⋯) in the following. The resulted signal components $S_d(t)$ can be modeled in amplitude modulation form as

$$S_d(t)=\sum_{e=1}^{E}\left\{1+\sum_{h=0}^{\infty}A_{dgeh}(t)\cos[2\pi\int hf_g(t)dt+\varphi_{dgeh}]\right\} c_{de}(t)\cos[2\pi f_{de}t+\psi_{de}], \tag{10}$$

where $c_{de}(t)$ stands for the time-varying amplitude, $A_{dgeh}(t)$ stands for the amplitude modulation coefficient, h denotes the harmonic order of fault frequency $f_g(t)$, and ψ_{de}, φ_{dgeh} are the corresponding initial phases. Equation (10) can further be expanded as (11).

$$S_d(t)=\sum_{e=1}^{E}\sum_{h=0}^{\infty}\frac{1}{2}A_{dgeh}(t)c_{re}(t)\left(\cos\left\{2\pi\int\left[f_{de}+hf_g(t)\right]dt+\psi_{de}+\varphi_{dgeh}\right\}+\cos\left\{2\pi\int\left[f_{de}-hf_g(t)\right]dt+\psi_{de}-\varphi_{dgeh}\right\}\right), \tag{11}$$

Therefore, when gear fault occurs, time-varying fault modulation sidebands $|f_{de}\pm hf_g(t)|$ (h=0, 1, 2⋯) are generated around the characteristic frequency f_{de}. It is worth noticing that f_{de} do not change with time, but their sidebands have time-varying instantaneous frequency. Such property help locate these characteristic frequencies in frequency domain. To facilitate the fault feature identification, the amplitude demodulation analysis can be conducted, and the time-varying gear fault frequency components are directly revealed.

Finally, considering all above factors, the measured torsional vibration signal is modeled as (12).

$$\begin{aligned} S(t) &= S_m(t)+S_r(t)+S_d(t) \\ &= \sum_{k=1}^{\infty}c_{mk}(t)a_{mk}(t)\cos[2\pi\int kf_m(t)dt+b_{mk}(t)+\psi_{mk}]+\sum_{i=1}^{\infty}c_r(t-t_i)\cos[2\pi f_r(t-t_i)+\psi_{ri}] \\ &\quad+\sum_{e=1}^{E}\left\{1+\sum_{h=0}^{\infty}A_{dgeh}(t)\cos[2\pi\int hf_g(t)dt+\varphi_{dgeh}]\right\}c_{de}(t)\cos[2\pi f_{de}t+\psi_{de}] \end{aligned}. \tag{12}$$

III. Multi-band Amplitude Demodulation Analysis

According to the derivations in Section 2, gear fault causes amplitude modulations on different carriers in the measured torsional vibration signal. Considering the fact that fault characteristics distribute in different frequency bands, the multi-band torsional vibration amplitude demodulation is proposed. Comparing with the conventional envelope spectrum analysis or narrow-band amplitude demodulation analysis, the proposed method can make full utilization of the fault characteristics distributed in different frequency bands, and meanwhile suppress random interferences for accurate fault recognition.

A. Envelope spectrum analysis

The envelope spectrum analysis directly reveals the amplitude modulation frequencies in relatively low frequency region, thus avoiding the identification of intricate fault modulation sidebands around the carrier frequency. However, it essentially only fits for analyzing mono-component signal with single carrier frequency, and interferences occur when the analyzed signal becomes more complex.

For a simple synthetic signal $x_1(t)$ with carrier frequency $f_{c1}(t)$ and amplitude modulation frequency $f_a(t)$, as

$$x_1(t)=[1+0.2\cos(2\pi\int f_a(t)\mathrm{d}t)]\cos[2\pi\int f_{c1}(t)\mathrm{d}t], \quad (13)$$

its amplitude envelope $\alpha_1(t)$ is derived as

$$\alpha_1(t)=\sqrt{x_1^2(t)+\mathrm{H}^2[x_1(t)]}=1+0.2\cos(2\pi\int f_a(t)\mathrm{d}t), \quad (14)$$

where H(·) denotes the Hilbert transform. Therefore, the amplitude envelope signal composes of only the amplitude modulation frequency $f_a(t)$.

For a synthetic signal $x_2(t)$ with two carrier frequencies $f_{c1}(t)$ and $f_{c2}(t)$, as

$$\begin{aligned}x_2(t)=&[1+0.2\cos(2\pi\int f_a(t)\mathrm{d}t)]\cos[2\pi\int f_{c1}(t)\mathrm{d}t]\\&+[1+0.2\cos(2\pi\int f_a(t)\mathrm{d}t)]\cos[2\pi\int f_{c2}(t)\mathrm{d}t]\end{aligned}. \quad (15)$$

Its amplitude envelope $\alpha_2(t)$ is derived as

$$\begin{aligned}\alpha_2(t)=&\left[1+0.2\cos(2\pi\int f_a(t)\mathrm{d}t)\right]\\&\cdot\sqrt{2+2\cos\left\{2\pi\int[f_{c1}(t)-f_{c2}(t)]\mathrm{d}t\right\}}\end{aligned}. \quad (16)$$

Therefore, more frequency components exist in the obtained envelope spectrum of $x_2(t)$, including the amplitude modulation frequency $f_a(t)$, the frequency harmonics of the difference between two carrier frequencies $f_{c1}(t)$-$f_{c2}(t)$, as well as their combinations.

For intuitive demonstration, we set $f_a(t)=20t+5$, $f_{c1}(t)=30f_a(t)$, $f_{c2}(t)=25f_a(t)$, and the results of envelope order spectrum analysis of $x_1(t)$ and $x_2(t)$ are shown in Fig. 1 for comparison.

Evidently, when more than one carrier frequencies exist in the analyzed signal, the frequency compositions of the amplitude envelope signal become more complex. As observed in Fig.1(a), the waveform of amplitude envelope signal $\alpha_2(t)$ shows more complex periodical features than that of $\alpha_1(t)$. These periodical details are further identified in the order spectrum plotted in Fig.1(b), as the integer harmonics of the difference between two carrier frequencies $p[f_{c1}(t)$-$f_{c2}(t)]$ (p=1, 2, 3⋯), and their combinations with the amplitude modulation frequency $p[f_{c1}(t)$-$f_{c2}(t)]\pm f_a(t)$. Unfortunately, these extra components complicate the order spectrum in Fig. 1(b), leaving it more difficult to intuitively identify the amplitude modulation frequency $f_a(t)$.

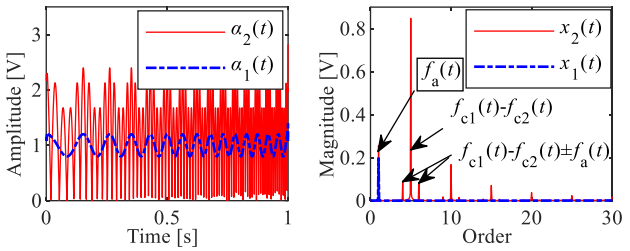

(a) (b)

FIGURE 1. Analysis of the synthetic signals $x_1(t)$ and $x_2(t)$. (a) waveforms of the amplitude envelope signal $\alpha_1(t)$ and $\alpha_2(t)$, (b) envelope order spectra of $x_1(t)$ and $x_2(t)$.

B. Narrow-band amplitude demodulation analysis

The narrow-band amplitude demodulation analysis focuses on single carrier frequency region for fault feature extraction. Yet under time-varying speed conditions, the adjacent carrier frequencies or their frequency sidebands often overlap in frequency domain. As a result, when the frequency region centered around the carrier frequency $f_{c1}(t)$ is selected for demodulation analysis, the frequency sidebands centered around the adjacent carrier frequency, or the independent rotating frequency orders, may also be mistakenly retained in the narrow-band filtered signal.

To study the interferences of independent frequency components in the narrow-band amplitude demodulation analysis, a synthetic signal $x_3(t)$ is constructed by adding a mono-component $f_b(t)$ to the synthetic signal $x_1(t)$, as

$$\begin{aligned}x_3(t)=&[1+0.2\cos(2\pi\int f_a(t)\mathrm{d}t)]\cos[2\pi\int f_{c1}(t)\mathrm{d}t]\\&+\cos[2\pi\int f_b(t)\mathrm{d}t]\end{aligned}. \quad (17)$$

Its amplitude envelope $\alpha_3(t)$ is then derived as

$$\begin{aligned}\alpha_3(t)=&\left\{[1+0.2\cos(2\pi\int f_a(t)\mathrm{d}t)]^2+2[1+0.2\cos(2\pi\int f_a(t)\mathrm{d}t)]\right.\\&\left.\cdot\cos\left\{2\pi\int[f_{c1}(t)-f_b(t)]\mathrm{d}t\right\}+1\right\}^{1/2}\end{aligned}. \quad (18)$$

Clearly, when a single frequency component $f_b(t)$ is mistakenly retained in the narrow-band filtered signal, the obtained amplitude envelope signal $\alpha_3(t)$ is more complex than the ideal case in (14). The extra frequency components relate to the carrier frequency $f_{c1}(t)$ and the added frequency $f_b(t)$, and

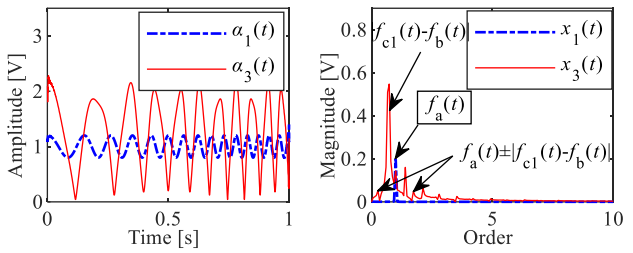

(a) (b)

FIGURE 2. Analysis of the synthetic signals $x_1(t)$ and $x_3(t)$. (a) waveforms of the amplitude envelope signal $\alpha_1(t)$ and $\alpha_3(t)$, (b) amplitude demodulated order spectra of $x_1(t)$ and $x_3(t)$.

may hinder the intuitive identification of the amplitude modulation frequency $f_a(t)$.

Set $f_a(t)=20t+5$, $f_{c1}(t)=30f_a(t)$, $f_b(t)=30.7f_a(t)$, the results of amplitude demodulation analysis of $x_1(t)$ and $x_3(t)$ are shown in Fig.2 for comparison. In Fig.2(a), the waveforms of $\alpha_1(t)$ and $\alpha_3(t)$ both show periodical features. Yet more components can be observed in the amplitude demodulated order spectrum of $x_3(t)$ than that of $x_1(t)$, as exhibited in Fig.2(b). The extra frequency components correspond to $p|f_{c1}(t)-f_b(t)|$ (p=1, 2, 3⋯) and $f_a(t)\pm|f_{c1}(t)-f_b(t)|$. Besides, the frequency component $|f_{c1}(t)-f_b(t)|$ becomes dominant in the amplitude demodulated order spectrum of $x_3(t)$, whereas the amplitude modulation frequency $f_a(t)$ has lower amplitude. As a result, even a single unwanted frequency component $f_b(t)$ leads to negative influence on the narrow-band amplitude demodulation.

C. Multi-band amplitude demodulation method for torsional vibration signal

The multi-band torsional vibration amplitude demodulation method is proposed in this work, to overcome the abovementioned interferences caused by coexistence of multiple carrier frequencies or other unwanted frequency components. Its main idea is to combine the fault modulation features shared in different modulation frequency regions, and meanwhile weakening the various interferences. The procedures are shown in Fig.3.

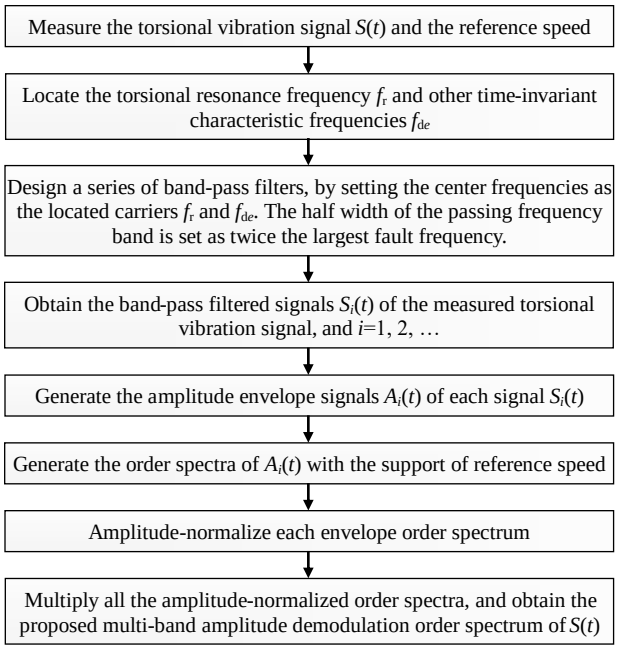

FIGURE 3. Procedure of the proposed multi-band torsional vibration amplitude demodulation method.

Essentially, a series of bandpass filters are designed and utilized for demodulation analysis within multiple frequency regions. The number of the demodulation frequency regions depends on the number of time-invariant frequency carriers. The bandpass frequency bands of the designed filters are decided based on central frequency and bandwidth. The central frequency is located as dominant peaks in the Fourier spectrum, since the resonance frequencies are time-invariant under time-varying speed conditions. The bandwidth is set as twice the largest fault frequency, to cover the time-varying fault modulation sidebands in frequency domain.

The novelty of the proposed method lies in the combined use of torsional resonance frequency band and device-related characteristic frequency bands for amplitude demodulation analysis. The time-invariant property of the carrier frequencies help localizes these demodulation frequency bands, and only the shared fault frequency components are enhanced. Besides, these frequency bands with constant carriers are narrower than the gear mesh frequency band, and less interferences are retained in the demodulation analysis. Such method is applicable when the rotating machinery fault causes amplitude modulation on the measured signal. The amplitude normalization of each envelope spectrum help balances the fault strength in each modulation frequency bands, thus realizing the fault feature integration. The achieved merits over conventional methods are further validated by numerical simulation and laboratory tests in the following.

IV. Numerical Simulation

The numerical simulated signal $S(t)$ of planetary gearbox torsional vibration is established according to the signal analytical model in (12). The gear mesh vibration, resonant vibration, and two extra components resulted from measurement device are considered in the simulation. Without loss of generality, only the fundamental frequencies are considered. The amplitude coefficients and modulation coefficients are set time-invariant for simplicity. All initial phases are set 0. $\varepsilon(t)$ at signal to noise ratio -1dB is added to mimic background noises. The numerical simulated signal $\varepsilon(t)$ is therefore written as

$$\begin{aligned} S(t) = {} & c_m\left\{1+A_{mg}\cos[2\pi\int f_g(t)dt+\varphi_{mg}]\right\} \\ & \cdot\cos\left\{2\pi\int f_m(t)dt+B_{mg}\cos[2\pi\int f_g(t)dt+\gamma_{mg}]+\psi_m\right\} \\ & +\sum_{i=1}^{\infty}c_r\exp[-2\pi\beta f_n(t-t_i)]\cos[2\pi f_r(t-t_i)+\psi_{ri}] \\ & \cdot D(t-t_i)+\sum_{e=1}^{2}\left\{1+A_{dge}(t)\cos[2\pi\int f_g(t)dt+\varphi_{dge}]\right\} \\ & \cdot c_{de}\cos[2\pi f_{de}t+\psi_{de}]+\varepsilon(t) \end{aligned} \quad , \quad (19)$$

TABLE I
COEFFICIENTS USED IN NUMERICAL SIMULATION

c_m	c_r	c_{d1}	c_{d2}	A_{mg}	A_{dg1}	A_{dg2}	B_{mg}	β
1	3	0.4	0.4	0.2	0.2	0.2	0.01	0.2

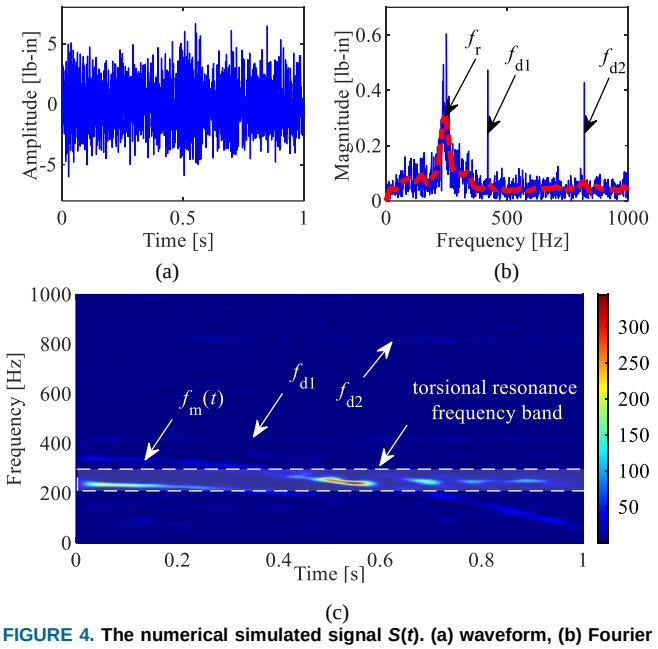

FIGURE 4. The numerical simulated signal $S(t)$. (a) waveform, (b) Fourier spectrum, (c) TFR.

where $D(\cdot)$ denotes the Heaviside function, and t_i stands for the time instance of fault impacts. The sun gear rotating frequency $f_s^{(r)}(t)$=-25t^2+30, the gear mesh frequency $f_m(t)$=11.39$f_s^{(r)}(t)$, and $f_s(t)$=2.63$f_s^{(r)}(t)$. The torsional resonance frequency f_r=250Hz, and two independent frequency are set as f_{d1}=420Hz and f_{d2}=820Hz. Other coefficients are listed in Table 1.

The waveform and Fourier spectrum of the constructed numerical simulated signal $S(t)$ are respectively plotted in Fig.4(a) and Fig.4(b). From the Fourier spectrum in Fig.4(b), we can observe the hillside-like spectral peak at around 250Hz, as well as two sharp spectral peaks at 420Hz and 820Hz. However, the fault-related modulation sidebands cannot be observed in Fig.4(b) due to the nonstationarity and noises. The time-frequency representation (TFR) of $S(t)$ is further generated by short time Fourier transform, as displayed in Fig.4(c). From the TFR, the time-varying gear mesh frequency component $f_m(t)$, the torsional resonance frequency band, and two time-invariant characteristic frequencies are clearly observed. The fault-induced modulation sidebands are indiscernible due to relatively low amplitude and noise interferences. To avoid the identification of time-varying fault frequency sidebands and directly reveal the fault frequency components, the amplitude demodulation analysis is applied.

To demonstrate the advantages of the proposed method, the envelope order spectra of both the original analyzed signal and the bandpass-filtered signals are firstly generated for comparison. Firstly, the waveform of the amplitude envelope of the simulated signal $S(t)$ is generated as plotted in Fig.5(a). Taking the sun gear rotating frequency $f_s^{(r)}(t)$ as the reference frequency, the envelope order spectrum is obtained as shown in Fig.5(b). In the order spectrum, the sun gear fault frequency $f_s(t)$ can be identified as order of 2.63. However, extra order component of 3.49 can also be observed with relatively high magnitude. According to Section 3, such interference results from the existence of more than one carrier frequencies in amplitude demodulation.

Then, the band-pass filtering is conducted before amplitude demodulation. Four demodulation frequency bands are selected for comparison. For gear mesh frequency band, the time-varying gear mesh frequency $f_m(t)$ and its modulation sidebands $f_m(t)\pm f_s(t)$, $f_m(t)\pm 2f_s(t)$ cover the range from 30Hz to 500Hz. For the torsional resonance frequency band, the frequency range of [f_r-2 $f_s(t)|_{max}$, f_r+2$f_s(t)|_{max}$], i.e., [92, 408]Hz, are selected for bandpass filtering. For the rest 2 demodulation frequency bands, their center frequencies correspond to the two time-invariant characteristic frequencies 420Hz and 820Hz, and their half bandwidths are set twice the maximum gear fault frequency $2f_s(t)|_{max}$. Therefore, frequency regions of [262, 578]Hz and [662, 978]Hz are analyzed.

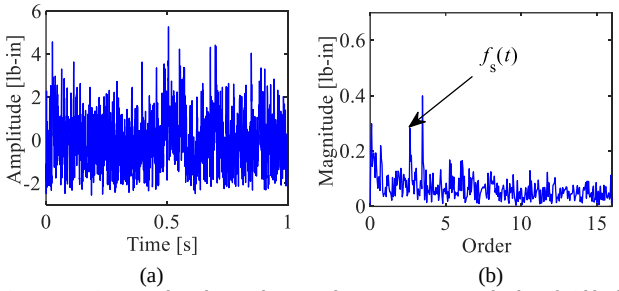

FIGURE 5. Conventional envelope order spectrum analysis of $S(t)$. (a) waveform of the amplitude envelope, (b) envelope order spectrum.

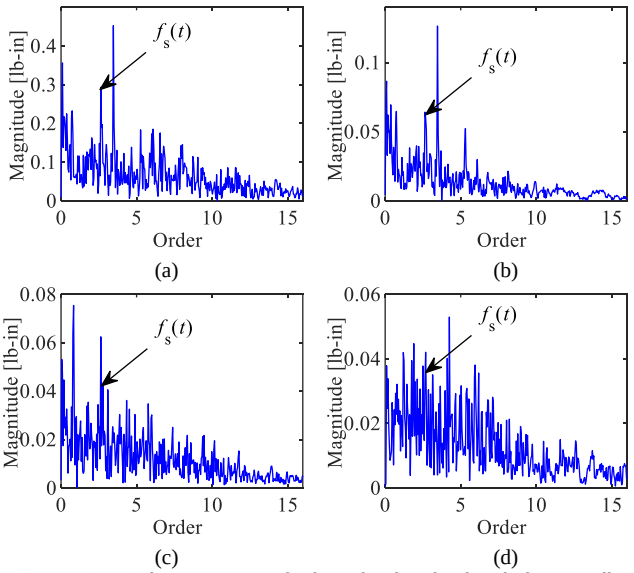

FIGURE 6. Order spectra of the simulated signal by amplitude demodulation within: (a) gear mesh frequency band of [30, 500]Hz, (b) torsional resonance frequency band of [92, 408]Hz, (c) characteristic frequency band of [262, 578]Hz, (d) characteristic frequency band of [662, 978]Hz.

The 4 order spectra of the bandpass filtered signals with different demodulation frequency bands are generated, as plotted in Fig.6(a)-(d). It is found that the order component corresponding to the sun gear fault frequency $f_s(t)$ can be found in all these 4 order spectra, but various interferences occur in different cases. In Fig.6(a) and 6(b), extra order component of 3.46 are observed at dominant magnitude. In Fig.6(c) and 6(d), the fault order component 2.63 has relatively low amplitude, and a series of weak spectral peaks can be misunderstood as meaningful components. According to the derivations in Section 3, these interference components result from more than one carrier frequency or extra frequency components in the demodulation frequency band.

In comparison, the proposed method makes use of the fault signatures in multiple demodulation frequency bands. Following the procedure in Fig.3, three carrier frequencies are located from the Fourier spectrum in Fig.4(b), as f_r =250Hz, f_{d1}=420Hz, and f_{d2}=820Hz. These frequency components do not vary with time under time-varying speed conditions, and are identified as carrier frequencies for multi-band amplitude demodulation. These carrier frequencies are set as the center frequencies of bandpass filters, and the half bandwidths are set twice the maximum gear fault frequency. The envelope order spectra of the obtained bandpass filtered signals are then generated and amplitude normalized. By multiplying the amplitude normalized envelope order spectra, the shared fault signatures are retained, whereas the various interferences components are suppressed. The obtained multi-band amplitude envelope order spectrum is exhibited in Fig.7. To quantitively evaluate the performance of fault signatures revelation, an indicator is designed as the magnitude of fault order 2.63 over the average magnitude of all the discrete order components from 0 to 10. Higher value of the indicator means more evident fault feature can be observed. The calculated indicators in different amplitude demodulation scenarios are shown in Fig.8 for comparison. Clearly, the indicator remains almost at same level even though different demodulation frequency bands are employed (scenario 1 to 5). By combining the fault signatures in multiple demodulation frequency bands (scenario 6), the fault order component can be prominently enhanced, whereas the interferences caused by complex frequency structure can be suppressed. In conclusion, the proposed method has potential use in revealing relatively weak gear fault signatures from complex nonstationary signals.

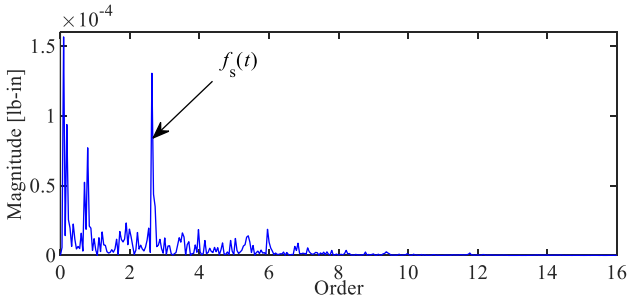

FIGURE 7. The proposed multi-band amplitude demodulated order spectrum of the simulated torsional vibration signal *S*(*t*).

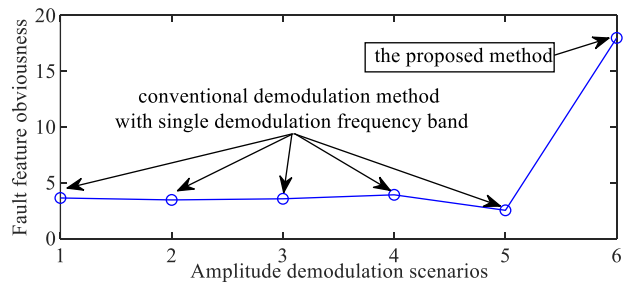

FIGURE 8. Comparisons of the capability of fault feature revelation by different amplitude demodulation scenarios.

V. Laboratory Experimental Verification

The proposed multi-band demodulation method makes utilization of the fault modulation features in both gear mesh frequency region and the resonance frequency regions. To validate its effectiveness in diagnosing gear defects in planetary gearbox, laboratory experiments are further conducted.

A. Experiment settings

The experiments are conducted on a planetary gearbox test rig shown in Fig.9. The ring gear of the one-stage planetary gearbox is fixed, and the transmission ratio is 8.1 (take sun gear as the input). Other gear configurations are listed in Table 2. A three-phase induction motor is connected to the input sun gear shaft to provide driving torque, and the output planet carrier shaft is connected to a magnetic powder brake to provide external load. To measure the torsional vibration, the PCB 4104-03A torque transducer is connected between the driving induction motor and the analyzed planetary gearbox. It is worth noticing that in real-world applications with limited mounting space, the motor current signals measured by current sensors may help support the torsional vibration evaluation [21-22]. The alternating voltage source at 3.24kHz is added on the torque transducer for signal measurement. The variable frequency drive is applied to realize the time-varying speed conditions.

Four groups of tests are conducted. In baseline case, all gears are theoretically in perfect condition. In faulty cases, local gear tooth defects are respectively added on the sun, planet, and ring gear, as shown in Fig.10. In all these four tests, the motor speed is set $f_i(t)=t+5$, and fixed load of 30 lb-in is added by the powder brake. The torsional vibration signals are measured by the torque transducer within 20 seconds at the sampling rate of 20kHz. Thus, the gear mesh frequency of the planetary gearbox is cast as $f_m(t)= 11.39\ f_s^{(r)}(t)$, and the planet carrier rotating frequency is cast as $f_c^{(r)}(t) = 0.12 f_s^{(r)}(t)$. The accurate motor speed is measured via encoder. In industrial applications, the time-varying instantaneous speed can also be estimated by vibration-based signal processing methods [23]. The rotating frequencies and fault frequencies of each gear in planetary gearbox are calculated as listed in Table 3.

TABLE II
PLANETARY GEARBOX CONFIGURATIONS

Gear	Sun (input)	Planet	Ring (fixed)
Number of gear teeth	13	38(3)	92

Note: The number of planet gears is indicated in the parenthesis.

TABLE III
PLANETARY GEARBOX CHARACTERISTIC FREQUENCIES

Gear	Sun	Planet	Ring
Rotation	$f_s^{(r)}(t) = f_i(t)$	$f_p^{(r)}(t) = 0.17 f_s^{(r)}(t)$	-
Fault	$f_s(t) = 2.63\, f_s^{(r)}(t)$	$f_p(t) = 0.29\, f_s^{(r)}(t)$	$f_r(t) = 0.37\, f_s^{(r)}(t)$

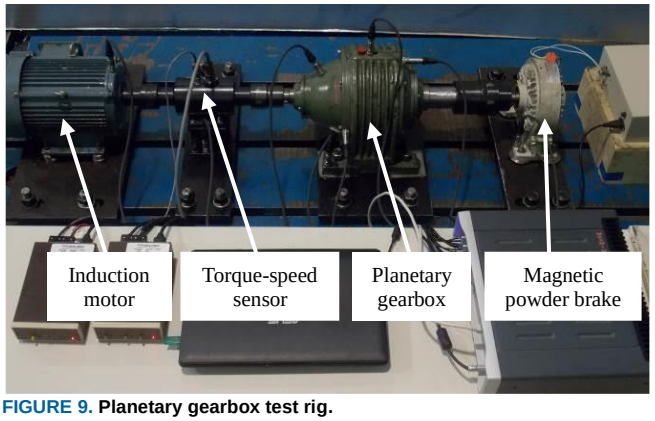

FIGURE 9. Planetary gearbox test rig.

(a) (b) (c)

FIGURE 10. Localized gear faults on: (a) sun gear, (b) planet gear, and (c) ring gear.

B. Baseline case

The waveform and Fourier spectrum of the measured planetary gearbox torsional vibration signal in baseline case are respectively plotted in Fig.11(a) and Fig.11(b). The motor speed is simultaneously measured as plotted in Fig.11(c). Although the characteristic frequencies are time-varying and show wide-band features in the Fourier spectrum, several time-invariant characteristic frequencies can be recognized as dominant peaks. As pinpointed in Fig.11(b), these 7 characteristic frequencies are identified as 44.5Hz, 144.9Hz, 438.9Hz, 737.8Hz, 1037.1Hz, 3248.3Hz, and 6495.9Hz. Since the spectral peak at 44.5Hz is hillside-like in the Fourier spectrum, it is considered as the torsional resonance frequency f_r. The 144.9Hz, 438.9Hz, 737.8Hz, and 1037.1Hz spectral peaks have equal frequency interval of around 300Hz. These characteristic frequency components show as discrete spectral peaks, and are judged as the electric signal components f_{d1}, f_{d2}, f_{d3}, and f_{d4}. The 3248.3Hz and 6495.9Hz correspond to the first and second harmonic of the power frequency 3.24kHz of the torque transducer. They are judged as the characteristic frequency component f_{d5} and f_{d6}.

Taking the sun gear rotating frequency $f_s^{(r)}(t)=f_i(t)$ as the basic order, the conventional envelope order spectrum of the baseline signal is generated as shown in Fig.11(d)-(e). Taking the gear mesh frequency band [30, 416]Hz as the passing frequency band, the narrow-band amplitude demodulated order spectrum is generated as shown in Fig.11(e). In both spectra, only the harmonics of sun gear rotating frequency $f_s^{(r)}(t)$ can be identified. In comparison, by combining the fault signatures in the detected 7 torsional vibration frequency bands, the order spectrum generated by the proposed multi-band torsional vibration amplitude demodulation method is shown in Fig.11(f). Clearly, the interferences are prominently diluted, and the proposed spectrum provide clear order peaks for accurate feature extraction. Still, only the harmonics of sun gear rotating frequency $f_s^{(r)}(t)$ and planet carrier rotating frequency $f_c^{(r)}(t)$ are observed, and fault signatures are not detected.

C. Sun gear fault diagnosis

In the sun gear fault case, only the healthy sun gear is replaced with a faulty one shown in Fig.10(a). The waveform and Fourier spectrum of the measured planetary gearbox torsional vibration signal are plotted in Fig.12(a)-(b), and the

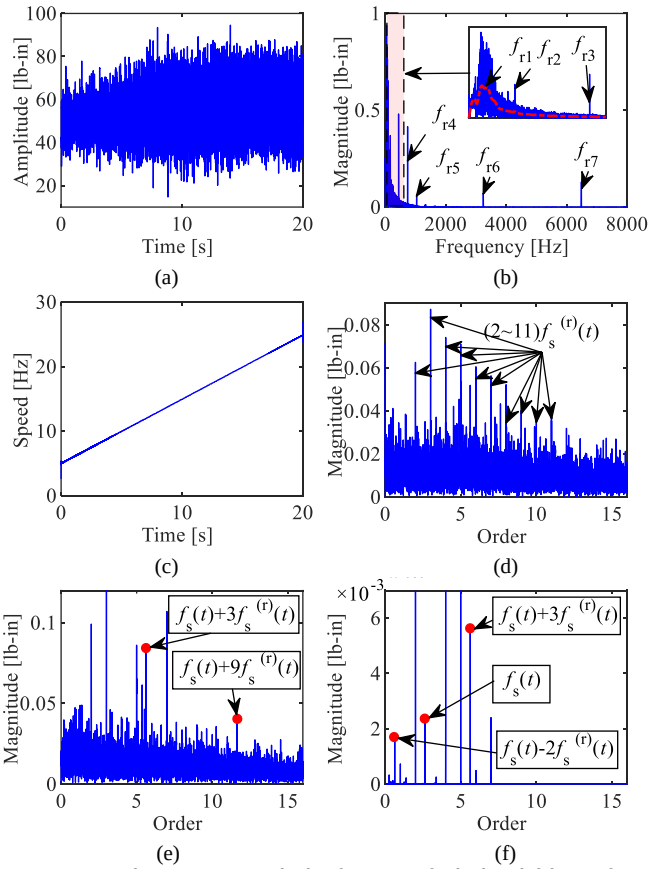

FIGURE 12. Order spectrum analysis of sun gear fault signal. (a) waveform, (b) Fourier spectrum, (c) motor speed, (d) envelope order spectrum, (e) narrow-band amplitude demodulated order spectrum, (f) multi-band torsional vibration amplitude demodulated order spectrum.

motor speed is plotted in Fig.12(c). Similar with the baseline case, a series of time-invariant characteristic frequencies can be estimated from the Fourier spectrum, as pinpointed in Fig. 12(b). Yet due to the time-varying characteristic frequencies, the fault signatures cannot be directly observed from the Fourier spectrum.

The envelope order spectrum analysis and narrow-band amplitude demodulation analysis are firstly applied on the sun gear fault signal. According to the obtained envelope order spectrum in Fig.12(d), only the harmonics of sun gear rotating frequency $f_s^{(r)}(t)$ are prominent, whereas other features are masked under noises. By band-pass filtering the analyzed signal through the gear mesh frequency region, and performing envelope spectrum analysis on the resulted signal, the narrow-band amplitude demodulated order spectrum is generated as shown in Fig.12(e). Owing to the band-pass filtering, less harmonics of $f_s^{(r)}(t)$ are observed, and two sun gear fault-related frequency components can be identified as $f_s(t)+3f_s^{(r)}(t)$ and $f_s(t)+9f_s^{(r)}(t)$.

The proposed multi-band torsional vibration amplitude demodulation analysis is then applied. Seven demodulation frequency bands centered at the detected time-invariant characteristic frequencies are utilized, and the obtained order spectrum is plotted in Fig.12(f). Clearly, the noise interferences are prominently eliminated since they have different frequency distributions in different torsional vibration frequency regions. Besides, the modulation frequency components shared in different frequency regions are enhanced and easier to be pinpointed. Owing to these two merits, the sun gear fault frequency $f_s(t)$ and its combinations with sun gear rotating frequency $f_s^{(r)}(t)$, i.e., $f_s(t)+3f_s^{(r)}(t)$ and $f_s(t)-2f_s^{(r)}(t)$ are intuitively presented in Fig.12(f). Comparing with the results in baseline case in Fig.11(f), the sun gear fault can be effectively diagnosed.

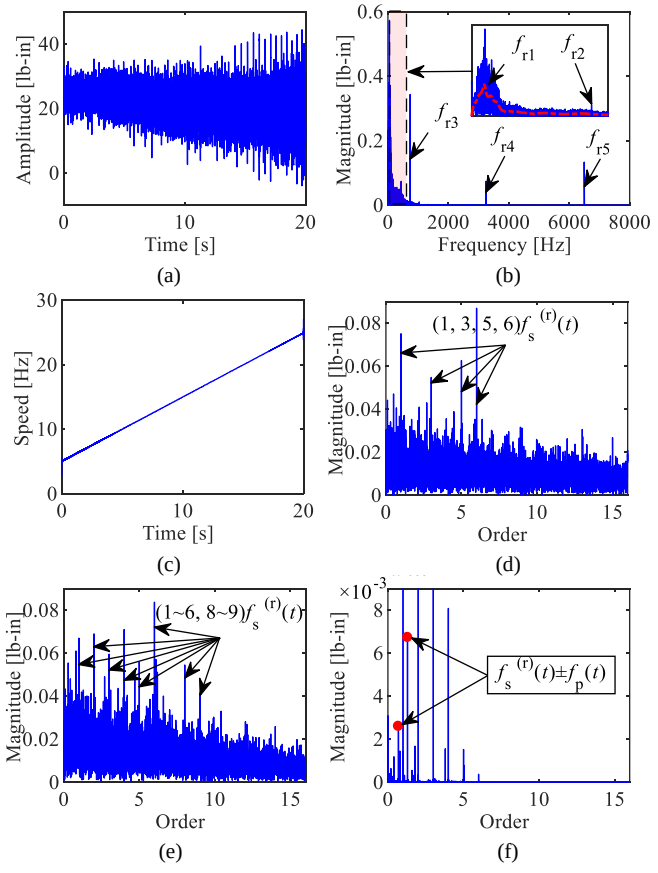

FIGURE 13. Order spectrum analysis of planet gear fault signal. (a) waveform, (b) Fourier spectrum, (c) motor speed, (d) envelope order spectrum, (e) narrow-band amplitude demodulated order spectrum, (f) multi-band torsional vibration amplitude demodulated order spectrum.

D. Planet gear fault diagnosis

Only one of the planet gears is replaced with a faulty one as shown in Fig.10(b), and other gears are theoretically healthy. The planetary gearbox torsional vibration signal and the motor speed are measured, as displayed in Fig.13(a)-(c).

The envelope order spectrum and the narrow-band amplitude demodulated order spectrum of the planet gear fault signal are generated as shown in Fig.13(d)-(e). However, only the harmonics of sun gear rotating frequency $f_s^{(r)}(t)$ are discernible in both spectra, and other details are masked. In comparison, the order spectrum generated by the proposed multi-band torsional vibration amplitude demodulation method is plotted in Fig.13(f). The noise interferences are effectively removed to highlight the characteristic frequency details. As a result, the combination of the planet gear fault frequency $f_p(t)$ and $f_s^{(r)}(t)$, i.e., $f_s^{(r)}(t)\pm f_p(t)$ are clearly identified. By comparing with the results in baseline case, the planet gear fault is successfully diagnosed.

E. Ring gear fault diagnosis

In ring gear fault case, one of the ring gear teeth is defected, as shown in Fig.10(c). The waveform and Fourier spectrum of the measured planetary gearbox torsional vibration signal are plotted in Fig.14(a)-(b), and the measured motor speed is plotted in Fig.14(c). 5 time-invariant characteristic frequencies are detected from the Fourier spectrum in Fig.14(b). To reveal the distribution of the time-varying modulation frequency features, the amplitude demodulation order spectrum analysis is then utilized.

The envelope order spectrum of the ring gear fault signal is shown in Fig.14(d). However, due to the existence of multiple carrier frequencies, independent rotating frequency orders and the background noise, only the dominant harmonics of the sun gear rotating frequency $f_s^{(r)}(t)$ can be pinpointed. After band-pass filtering the analyzed signal in gear mesh frequency region, the narrow-band filtered signal is generated, and its amplitude demodulated order spectrum is plotted in Fig.14(e). Although the harmonics of $f_s^{(r)}(t)$ are to some extent eliminated, other features are still masked under noise interferences.

The proposed multi-band torsional vibration amplitude demodulated order spectrum is then generated and exhibited in Fig.14(f). Clearly, the unwanted noise interferences are effectively eliminated. Although the fault signatures are relatively unobvious, we can still detect the order peak

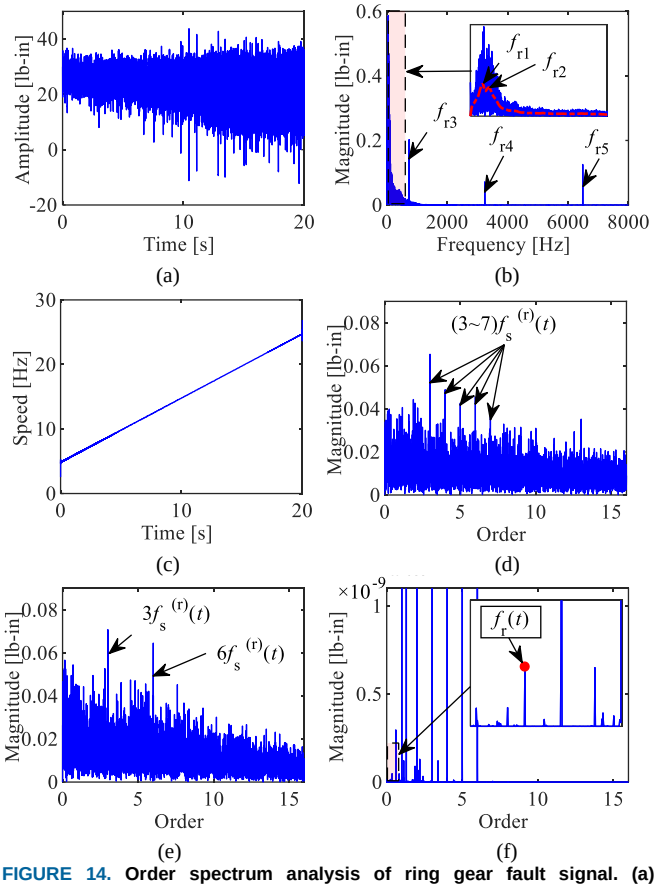

FIGURE 14. Order spectrum analysis of ring gear fault signal. (a) waveform, (b) Fourier spectrum, (c) motor speed, (d) envelope order spectrum, (e) narrow-band amplitude demodulated order spectrum, (f) multi-band torsional vibration amplitude demodulated order spectrum.

corresponding the ring gear fault frequency $f_r(t)$ in the zoomed-in view of Fig.14(f). Comparing with the results in baseline case, the ring gear fault is effectively diagnosed.

VI. Conclusions

Two contributions are made in this work for planetary gearbox fault feature extraction. Firstly, via analytical modeling of the planetary gearbox torsional vibration response, the gear fault modulation sidebands are revealed to distribute around not only the gear mesh frequency but also the torsional resonance frequencies. Secondly, by integrating the fault characteristics among various frequency regions, the proposed multi-band demodulation method outperforms conventional envelope spectrum and narrow-band amplitude demodulation spectrum in revealing relatively-weak fault features. The results of both numerical simulation and laboratory experiments validate the advantages of the proposed method in diagnosing sun, planet and ring gear faults under time-varying speed conditions. Since the revelation of the time-varying amplitude of the fault signatures cannot be realized in the proposed order spectrum, further studies in time-frequency domain are expected. Studies on adaptive optimization of the bandwidth will also be conducted in the future.

References

[1] M. Inalpolat and A. Kahraman, "A theoretical and experimental investigation of modulation sidebands of planetary gear sets," *Journal of Sound and Vibration*, vol. 323, pp. 677–696, Jan. 2009.

[2] T. Y. Wang, Q. K. Han, F. L. Chu, and Z. P. Feng, "Vibration based condition monitoring and fault diagnosis of wind turbine planetary gearbox: A review," *Mechanical Systems and Signal Processing*, vol. 126, pp. 662–685, Jul. 2019.

[3] G. G. Escudero, P. Bo, H. González-Barrio, et al. "5-axis double-flank CNC machining of spiral bevel gears via custom-shaped tools—Part II: physical validations and experiments," *Int J Adv Manuf. Technol.* vol. 119, pp. 1647–1658, Nov. 2021.

[4] Y. Xu, X. Tang, G. Feng, D. Wang, C. Ashworth, F. Gu, and A. Ball. "Orthogonal on-rotor sensing vibrations for condition monitoring of rotating machines," *Journal of Dynamics, Monitoring and Diagnostics*, vol.1 pp. 29-36, Mar. 2022.

[5] S. Xue and I. Howard, "Torsional vibration signal analysis as a diagnostic tool for planetary gear fault detection," *Mechanical Systems and Signal Processing*, vol. 100, pp. 706–728, Feb. 2018.

[6] M. H. Marzebali, J. Faiz, G. A. Capolino, S. H. Kia, and H. Henao, "Planetary gear fault detection based on mechanical torque and stator current signatures of a wound rotor induction generator," *IEEE Transactions on Energy Conversion*, vol. 33, pp. 1072–1085, Sep. 2018.

[7] M. M. Zhao and J. C. Ji, "Nonlinear torsional vibrations of a wind turbine gearbox," *Applied Mathematical Modelling*, vol. 39, pp. 4928–4950, Aug. 2015.

[8] Z. P. Feng and M. J. Zuo, "Vibration signal models for fault diagnosis of planetary gearboxes," *Journal of Sound and Vibration*, vol. 331, pp. 4919–4939, Oct. 2012.

[9] Y. G. Lei, Z. Y. Liu, J. Lin, and F. B. Lu, "Phenomenological models of vibration signals for condition monitoring and fault diagnosis of epicyclic gearboxes," *Journal of Sound and Vibration*, vol. 369, pp. 266–281, May. 2016.

[10] G. L. He, K. Ding, W. H. Li, and Y. Z. Li, "Frequency response model and mechanism for wind turbine planetary gear train vibration analysis," *IET Renewable Power Generation*, vol. 11, pp. 425–432. Mar. 2017.

[11] Z. P. Feng and M. J. Zuo, "Fault diagnosis of planetary gearboxes via torsional vibration signal analysis," *Mechanical Systems and Signal Processing*, vol. 36, pp. 401–421, Apr. 2013.

[12] X. W. Chen and Z. P. Feng, "Time-frequency analysis of torsional vibration signals in resonance region for planetary gearbox fault diagnosis under variable speed conditions," *IEEE Access*, vol. 5, pp. 21918–21926, Jan. 2017.

[13] Z. P. Feng, X. W. Chen, M. Liang, and F. Ma, "Time-frequency demodulation analysis based on iterative generalized demodulation for fault diagnosis of planetary gearbox under nonstationary conditions," *Mechanical Systems and Signal Processing*, vol. 62, pp. 54–74, Oct. 2015.

[14] P. Borghesani and J. Antoni, "CS2 analysis in presence of non-Gaussian background noise – Effect on traditional estimators and resilience of log-envelope indicators," *Mechanical Systems and Signal Processing*, vol. 90, pp. 378–398, Jun. 2017.

[15] T. Barszcz, R. B. Randall, "Application of spectral kurtosis for detection of a tooth crack in the planetary gear of a wind turbine," *Mechanical Systems and Signal Processing*, vol. 23, pp. 1352–1365, May. 2009.

[16] L. M. Wang, Y. M. Shao, and Z. Cao, "Optimal demodulation subband selection for sun gear crack fault diagnosis in planetary gearbox," *Measurement*, vol. 125, pp. 554–563, Sep. 2018.

[17] W. Y. Wang, "Early detection of gear tooth cracking using the resonance demodulation technique," *Mechanical Systems and Signal Processing*, vol. 15, pp. 887–903, Sep. 2001.

[18] F. Olver, D. Lozier, R. F. Boisvert, and C. W. Clark, Handbook of Mathematical Functions, Cambridge University Press, New York, 2010.

[19] R. B. Randall and J. Antoni, "Rolling element bearing diagnostics-A tutorial," *Mechanical Systems and Signal Processing*, vol. 25, pp. 485–520, Feb. 2011.

[20] L. Xu, K. Ding, G. L. He, Y. Z. Li, and Z. Y. Chen, "Resonance modulation vibration mechanism of equally-spaced planetary gearbox

with a localized fault on sun gear," *Mechanical Systems and Signal Processing*, vol. 166, 108450, Mar. 2022.

[21] S. Kia, H. Henao, and G. Capolino, "Torsional vibration assessment using induction machine electromagnetic torque estimation," *IEEE Transactions on Industrial Electronics*, vol. 57, no. 1, pp. 209–219, Jan. 2010.

[22] X. Chen and Z. Feng, "New schemes of induction motor electric signature analysis for gear fault diagnosis: a comparative study", *IEEE Transactions on Power Electronics*, vol. 39, no. 3, pp. 3590–3600, Mar. 2024.

[23] S. Lu, R. Yan, Y. Liu, and Q. Wang, "Tacholess speed estimation in order tracking: a review with application to rotating machine fault diagnosis," *IEEE Trans. Instrum. Meas.*, vol. 68, no. 7, pp. 2315–2332, Jul. 2019.

Xiaowang Chen received the B.S. degree in vehicle engineering in 2013, and the Ph.D. degree in mechanical engineering in 2018, both from University of Science and Technology Beijing. From 2016 to 2017, he was a visiting Ph.D. student in department of mechanical engineering, University of Alberta. He was selected in Young Elite Scientists Sponsorship Program by China Association for Science and Technology in 2022. Currently, he is an associate professor with the school of mechanical engineering, University of Science and Technology Beijing. His research interests include electric-drivetrain fault diagnosis and signal processing.

Yubo Sun received the B.S. degree in vehicle engineering in 2023 from Guangxi University. Currently, he is a post-graduate student at the School of Mechanical Engineering, University of Science and Technology Beijing. His research interests include machinery fault diagnosis and signal processing.

Ying Zhang (Member, IEEE) is currently an Associate Professor with the School of Mechanical Engineering, University of Science and Technology Beijing. She received the bachelor's degree and master's degree from the College of Mechanical and Electrical Engineering, Beijing University of Chemical Technology, China, in 2014 and 2017, respectively. She completed the Ph.D. degree with the School of Mechanical and Mechatronic Engineering, University of Technology Sydney, Australia in 2021. From 2021 to 2023, she was a postdoctoral fellow with Department of Industrial Engineering, Tsinghua University, China. Her main research interests include intelligent fault diagnosis of industrial machinery, machine learning, prognostics and health management. She is also a reviewer of more than ten international journals.

Zhipeng Feng (Member, IEEE) received the B.S. degree in automotive engineering from Jilin University in 1997, the M.S. degree in mechanical engineering from Kunming University of Science and Technology in 2000, and the Ph.D. degree in power machinery engineering from Dalian University of Technology, China in 2003. From 2003 to 2005, he was a postdoctoral fellow with Department of Precision Instruments and Mechanology, Tsinghua University, China. From 2006 to 2007, he was a postdoctoral research fellow with Department of Mechanical Engineering, University of Alberta, Canada. Currently, he is a professor with School of Mechanical Engineering, University of Science and Technology Beijing, China. His research interests include machinery fault diagnosis, signal processing, electromechanical system dynamics, and artificial intelligence.